ARTICLE | Article in Press

Dual inhibition of BChE and Aβ42 aggregation by novel 2-phenylbenzofuran derivatives as a multitarget approach to Alzheimer's disease

Giovanna Lucia Delogu · Michela Begala · Manuel Novás · Maria João Matos · Paola Caria · Daniela Virginia Frau · Valeria Sogos · Michela Isola · Cinzia Sanna · Carlo Giovanni Ignazio Tuberoso · Antonella Fais · Benedetta Era · Sonia Floris · Francesca Pintus

Received: 16 September 2026 / Accepted: 3 November 2026
© The Author(s) 2026

Abstract

Alzheimer's disease (AD) is a complex neurodegenerative disorder involving multiple pathogenic mechanisms, requiring therapies targeting different pathways. In this study, five 2-phenylbenzofurans (**8**–**12**) were designed, synthesized *via* the Wittig reaction, and evaluated as potential multi-target agents for AD. All compounds selectively inhibited butyrylcholinesterase (BChE, IC_{50} = 5.1–45.8 μM), with compounds **8** and **12** showing the highest activity, better than the reference compound. All compounds also exhibited significant antioxidant activity in the ABTS assay (EC_{50} = 10.65–27.02 μM), with compound **12** displaying the highest antioxidant capacity, outperforming the reference standard. Both compounds act as mixed-type BChE inhibitors and were non-cytotoxic in SH-SY5Y neuroblastoma cells at their active concentrations. Moreover, they significantly decreased intracellular reactive oxygen species levels induced by H_2O_2, with compound **12** demonstrating highest potency. Thioflavin-T assay proved that both compounds effectively interfere with Aβ42 aggregation, with compound **12** showing the strongest anti-amyloid activity. The biological findings were further supported by computational studies, with molecular docking providing insight into BChE binding and ADMET analysis predicting favourable pharmacokinetic properties. Preliminary telomere analyses further suggested protection against oxidative stress-induced chromosomal damage. Overall, compound **12** emerges as the most promising molecule for further optimization as a multitarget therapeutic agent for AD.

Keywords Acetylcholinesterase · Butyrylcholinesterase · Benzofurans synthesis · Enzyme inhibition · Alzheimer's disease · Telomeres · Aβ42

This Article in Press is shared early to give you faster access to new research. It is citable and carries a permanent DOI. The final edited version will replace it automatically.

https://doi.org/10.1038/s41598-026-79845-9

Published online: 06 November 2026

scientific reports

Introduction

Alzheimer's disease (AD) is a neurodegenerative condition closely linked to aging and associated with synaptic impairment and progressive neuronal degeneration in specific brain regions essential for memory and cognitive function. It represents the predominant cause of dementia worldwide, with prevalence projected to increase considerably in the coming decades[1].

Cholinergic dysfunction is one of the key pathological features of AD, given the central role of cholinergic signalling in memory and learning processes. In AD, degeneration of cholinergic neurons results in a reduction of acetylcholine (ACh) levels, contributing to cognitive impairment[2].

Butyrylcholinesterase (BChE) is a member of the cholinesterase (ChE) enzyme family involved in the regulation of cholinergic signaling. It is a non-specific enzyme widely distributed in the body and capable of hydrolyzing various choline esters, including ACh. In healthy brains, BChE plays a secondary role in ACh metabolism, but its activity gradually increases with AD progression, particularly during the later stages of the disease. This increase underscores BChE's growing contribution to cholinergic dysfunction and supports its relevance as a therapeutic target[3].

Considering the decreased production of ACh due to neuronal death and increased ChE activity, ChE inhibition is considered a compelling strategy for the symptomatic management of AD. In particular, targeting BChE may offer advantages in the advanced stages of the disease, when its activity becomes more prominent[4].

In parallel with cholinergic dysfunction, AD is defined by two major pathological hallmarks, consisting of neurofibrillary tangles due to hyperphosphorylated tau protein and amyloid-beta (Aβ) plaques produced through the enzymatic processing of the amyloid precursor protein. Aβ undergoes gradual aggregation, forming soluble oligomers and fibrils that can result in the deposition of insoluble plaques in the brain, especially in the blood vessels and cortex. These aggregates interfere with neuronal communication and trigger neuroinflammatory responses, contributing to neuronal loss and disease progression[5].

The pathological process associated with AD are exacerbated by oxidative stress. An excess of reactive oxygen species (ROS) leads to lipid peroxidation and cellular injury, impairing neuronal function and reducing neurotransmitter production, including ACh. This creates a vicious cycle that amplifies both cholinergic deficits and amyloid-related toxicity, ultimately accelerating neurodegeneration[6].

In this context, AD is increasingly recognized as a multifactorial disorder, with multiple pathological mechanisms synergistically contributing to neurodegeneration. This complexity has led to a transition from single-target strategies to the development of multi-target-directed ligands (MTDLs), which are able to act on multiple pathological targets simultaneously[7]. In addition to cholinergic deficit and amyloid deposition, oxidative stress is a key contributor to neuronal damage and functional decline. ROS can induce oxidative DNA damage, leading to telomeric instability and accelerated telomere shortening[8]. Under physiological conditions, telomeres progressively shorten with each cell division, ultimately resulting in replicative senescence. However, oxidative stress significantly accelerates this process. Conversely, antioxidant mechanisms may contribute to slowing telomere attrition, thereby contributing to cellular protection. Within this framework, identifying compounds that combine ChE inhibition with antioxidant activity may indirectly protect telomere integrity.

Therefore, molecules with dual or multiple activities, including anti-amyloid aggregation properties, antioxidant effects, and ChE inhibition, represent promising candidates for the MTDL strategy, with the potential to develop more effective therapeutic approaches for AD.

Our research group has long been engaged in the development of cholinesterase inhibitors as potential therapeutic agents for AD. In this context, we previously designed, synthesised, and biologically evaluated a series of hydroxylated 2-phenylbenzofuran derivatives[9–14]. The experimental data indicated that most tested benzofurans displayed selective BChE inhibition, with inhibitory potency varying substantially among the derivatives. This experimental evidence agrees with theoretical studies, which support the observed selectivity and inhibitory activity at the molecular level.

A bromine substituent at the 7-position of the benzofuran scaffold, combined with *meta*-hydroxylation on the 2-phenyl ring, strongly enhances BChE inhibitory activity. This research advances understanding of this scaffold, showing the influence of variations in the number and position of halogen atoms, hydroxyl and methyl groups on the properties of the 2-phenylbenzofuran nucleus.

Materials and methods

Chemistry

Starting materials, solvents, and reagents used for the synthesis of target compounds were purchased from available sources and used without further purification. The reaction was monitored by thin-layer chromatography (TLC) on silica gel 60 F254 plates, and products were purified by column chromatography using silica gel. Melting points were determined on a Stuart Scientific SMP 11 melting point apparatus. NMR spectra were recorded with a Bruker Avance III HD 600 spectrometer (600 MHz for ^{1}H,150.8 MHz for ^{13}C). Chemical shifts are reported in ppm (δ) relative to tetramethylsilane (TMS) as an internal standard. GC-MS and HRSM analyses were performed using the instrumentation described in the Supplementary Material. Detailed synthetic procedure, purification conditions, compound characterization, and complete spectroscopic data including NMR characterization, are provided in the Supplementary Material.

Biological activity

Enzyme inhibition

ChE inhibitory activity was evaluated against acetylcholinesterase from *Electrophorus electricus* (AChE, EC 3.1.1.7) and BChE (EC 3.1.1.8) from equine serum using the Ellman's colorimetric assay. Galantamine served as a positive control under identical conditions[12]. Kinetic analysis was performed using Lineweaver–Burk double-reciprocal plots. See Supplementary Materials for full details.

ABTS assay

The antioxidant activity of the tested compounds was determined using the ABTS radical cation ($ABTS^{+\cdot}$) method[12]. Full experimental protocol is available in Supplementary Materials.

Cell culture and intracellular ROS levels

The human neuroblastoma cell line (SH-SY5Y) was purchased from Professor Sogos (University of Cagliari, Italy) at the ICLC cell Bank (cat. # HTL95013) and cultured under previously reported conditions[14]. Cells were treated with compounds at different concentrations for 24 h. Cell viability was then determined by MTT assay. Intracellular ROS levels in the absence or presence of compounds were measured using the 2',7'-dichlorodihydrofluorescein diacetate assay[15]. Cells were cultured in 96-well plates and exposed to varying compound concentrations for 24 h. Subsequently, cells were incubated with 2 mM H_2O_2 to induce oxidative stress and changes in fluorescence were monitored every 5 min for 60 min using a microplate reader (excitation 485 nm; emission 530 nm).

Telomere length and quantitative fluorescent in situ hybridization

To assess telomere length, quantitative fluorescence in situ hybridization (Q-FISH) was performed on SH-SY5Y cells treated with compounds **8** and **12**, using a FITC-labeled telomeric PNA probe, as previously described[16]. The experimental protocol is available in the Supplementary Materials.

ThT assay

Thioflavin T (ThT), a benzothiazole dye, has been extensively used to detect and quantify the amyloid fibrils in vitro and represents a well-established method to monitor amyloid-beta (Aβ) fibrillation kinetics in real time. In presence of β-sheet-rich structures, such as the cross-β-sheet arrangement typical of Aβ fibrils, ThT exhibits an enhancement of fluorescence along with a characteristic blue shift. The excitation and emission maxima were observed at approximately 440 and 490 nm, respectively[13,17]. Because ThT binds amyloid fibrils in a stoichiometric and saturable manner, the fluorescence signal of the Aβ-ThT complex can be used to quantitatively assess fibril formation. Fluorescence spectra are recorded over time, and intensity values are plotted as a function of time to obtain aggregation curves. Deviations from the control sample, consisting of Aβ aggregation in the absence of any compound, may indicate inhibition or acceleration of the aggregation process. The experimental protocol is available in the Supplementary Materials.

Transmission electron microscope preparation

Approximately 30 µL of each sample was deposited onto nickel grids previously coated with a 90 nm layer of EPON resin (Glycide Ether 100; Merck, Darmstadt, Germany) to prevent sample loss through the grid mesh. The grids were air-dried overnight at room temperature and subsequently fixed with a 1% osmium solution for 10 min. Following fixation, the grids were washed with distilled water and left to air-dry overnight at room temperature. Ultrastructural observations were then carried out using a JEOL JEM 1400 Plus transmission electron microscope.

Computational method

ADME prediction

ADME (absorption, distribution, metabolism, excretion) and toxicity-related aspects of the compounds were predicted using SwissADME and ADMETlab 3.0[18,19].

Molecular docking

Coordinates for human butyrylcholinesterase were taken from PDB entry 4TPK, and chain A was used throughout. Receptor preparation was carried out in CHARMM: crystallographic ligands were deleted, incomplete side chains were rebuilt, hydrogens were added, and ionisable residues were assigned protonation states corresponding to pH 7.4. Water molecules were discarded except where a water bridged the ligand and an active-site residue in the crystal structure.

Compounds 8 and 12 were built from SMILES strings in Open Babel, protonated at pH 7.4, and energy-minimised in three dimensions under the MMFF94 force field. Gasteiger charges were then assigned to both ligands. The docking box (20 × 20 × 20 Å) was positioned over the orthosteric site, taking its centre from the co-crystallised ligand *N*-((1-(2,3-dihydro-1 H-inden-2-yl)piperidin-3-yl)methyl)-*N*-(2-methoxyethyl)-2-naphthamide at (7,12,11). Poses were generated with AutoDock Vina v1.2.5 at an exhaustiveness of 64, run through the Vina Python API under Python 3.8 via the SwissDock interface. Contacts in the top-ranked poses (hydrogen bonds,

π–π stacking and hydrophobic interactions) were assigned with PLIP v2025[20]. Figures of the bound poses and their interaction maps were prepared in PyMOL 3.10 at 300 dpi.

Statistical analysis

Data are reported as mean ±standard deviation (SD). Group comparisons were carried out using one-way ANOVA followed by Tukey's post hoc test, using GraphPad Prism version 8 (San Diego, CA, USA). Results were considered statistically significant with a p-value < 0.05.

Results and discussion

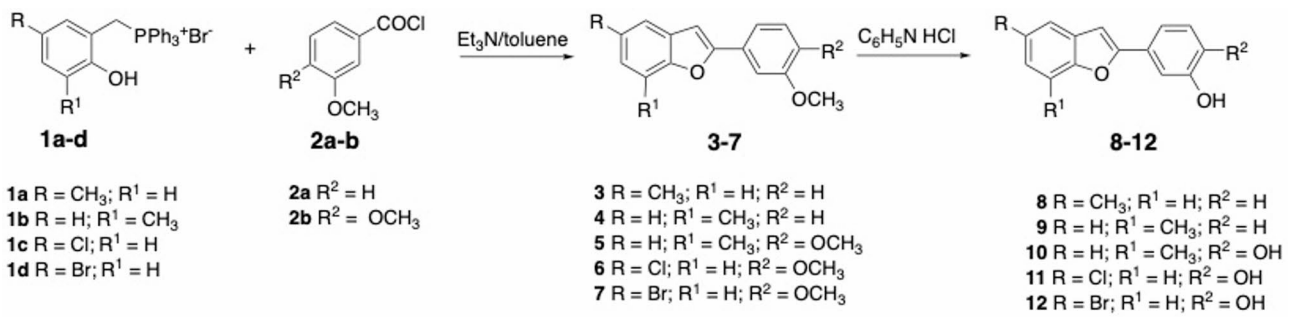
Chemistry

Scheme 1 shows the synthetic route to obtain benzofuran derivatives. An intramolecular Wittig reaction efficiently yields methoxylated derivatives. Wittig reagents **1a-d**, obtained by reacting 2-hydroxybenzyl alcohols with triphenylphosphine hydrobromide, were subsequently treated with methoxybenzoyl chloride **2a–b** to yield methoxyphenylbenzobenzofurans **3–7**. Hydroxyphenylbenzofurans **8–12** are obtained in near-quantitative yields by heating the corresponding methoxylated benzofurans with pyridine hydrochloride under microwave irradiation (300 W) for 10–15 min[9–14]. The structures of the synthesized compounds were elucidated using comprehensive spectral data. (see Supplementary Material for details).

Biological activity

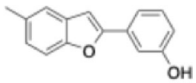
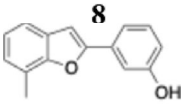
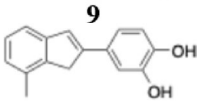
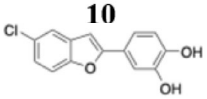
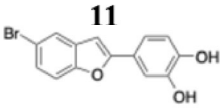
Enzyme inhibition and antioxidant activity

To assess compound inhibitory activity against ChE, we used commercial enzymes with high homology to the corresponding human enzymes: acetylcholinesterase (AChE) from *Electrophorus electricus* and BChE from equine serum. These sources of enzyme represent in vitro models frequently used for screening studies to evaluate anticholinesterase activity. IC_{50} values were calculated for compounds displaying at least 50% inhibition at 100 µM. Table 1 reports the corresponding inhibitory activities. None of the analyzed compounds demonstrated a significant capacity to inhibit AChE activity. In contrast, all compounds displayed BChE inhibitory activity with varying degrees of potency, with IC_{50} values in the range of 5.1–45.8 µM. Notably, compounds **8** ($IC_{50} = 5.1$ µM) and **12** ($IC_{50} = 16.0$ µM) demonstrated greater inhibitory activity against BChE, with approximately 5.5-fold and



Scheme 1 Synthesis of 2-hydroxyphenylbenzofurans **8–12**.

Table 1 ChE inhibitory activity and antioxidant capacity of compounds **8**–**12**.

Compound	AChE IC_{50} µM	BChE IC_{50} µM	ABTS EC_{50} µM
	> 100	5.1 ± 0.09	27.02 ± 2.26
8 	> 100	26.0 ± 1.98	14.15 ± 0.07
9 	> 100	45.8 ± 1.27	12.30 ± 0.42
10 	> 100	38.2 ± 3.39	17.05 ± 0.21
11 	> 100	16.0 ± 0.70	10.65 ± 1.77
12			
Galantamine	3.12 ± 0.15	28.06 ± 2.10	
Trolox			13.0 ± 1.1

1.8-fold higher potency ($p < 0.0001$), respectively, compared to the reference inhibitor galantamine ($IC_{50} = 28.06$ µM).

In addition to ChE inhibition, the antioxidant capacity of the tested compounds was assessed by the ABTS assay. All compounds exhibited measurable activity, with EC_{50} values in the range of 10.65–27.02 µM. Compound **12** showed the strongest antioxidant capacity ($EC_{50} = 10.65 \pm 1.77$ µM), followed by **10** (12.30 ± 0.42 µM) and **9** (14.15 ± 0.07 µM). Notably, compounds **10** and **12** demonstrated the best antioxidant activity, comparable to the reference standard Trolox ($EC_{50} = 13.0 \pm 1.1$ µM), indicating good radical scavenging potential. In contrast, compound **8** displayed the weakest activity of the series ($EC_{50} = 27.02 \pm 2.26$ µM).

Results are expressed as the mean ± standard deviation from three independent assays.

Benzofuran **8** emerged as the most potent BChE inhibitor, whereas benzofuran **12** exhibited the most favorable overall profile, combining significant BChE inhibitory activity with the strongest antioxidant capacity in the ABTS assay.

Based on these findings, compounds **8** and **12** were selected for further studies. Enzyme kinetic studies were subsequently conducted to elucidate their mode of inhibition. Enzymatic activity was measured at different substrate and inhibitor concentrations. As illustrated by the Lineweaver-Burk plot (Fig. 1), the reciprocal reaction rate (1/V) was related to the reciprocal substrate concentration (1/[S]).

Figure 1A shows the Lineweaver–Burk plots obtained for compound **8**. The intersection of the lines in the second quadrant is consistent with a mixed-type pattern, suggesting that binding occurs to the free enzyme (E) and the enzyme–substrate (ES) state. Secondary plots (Fig. 1B and C) were constructed by plotting the slope of the Lineweaver–Burk plots and 1/Vmax against the inhibitor concentration. These plots allowed the determination of the inhibition constants of 1.5 µM (Ki) and 6.4 µM (K_{IS}) for the uncomplexed enzyme and the enzyme–substrate complex, respectively. Similar results were obtained for compound **12**, which also exhibited a mixed-type inhibition mechanism (Fig. 2A) with a Ki value of 6.3 µM and a K_{IS} value of 25.9 µM (Fig. 2B and C).

Interestingly, the K_{IS} values are approximately 4 times higher than their respective K_I values for both compounds. This indicates that both inhibitors possess approximately 4-fold greater affinity for free BChE than for the enzyme-substrate complex.

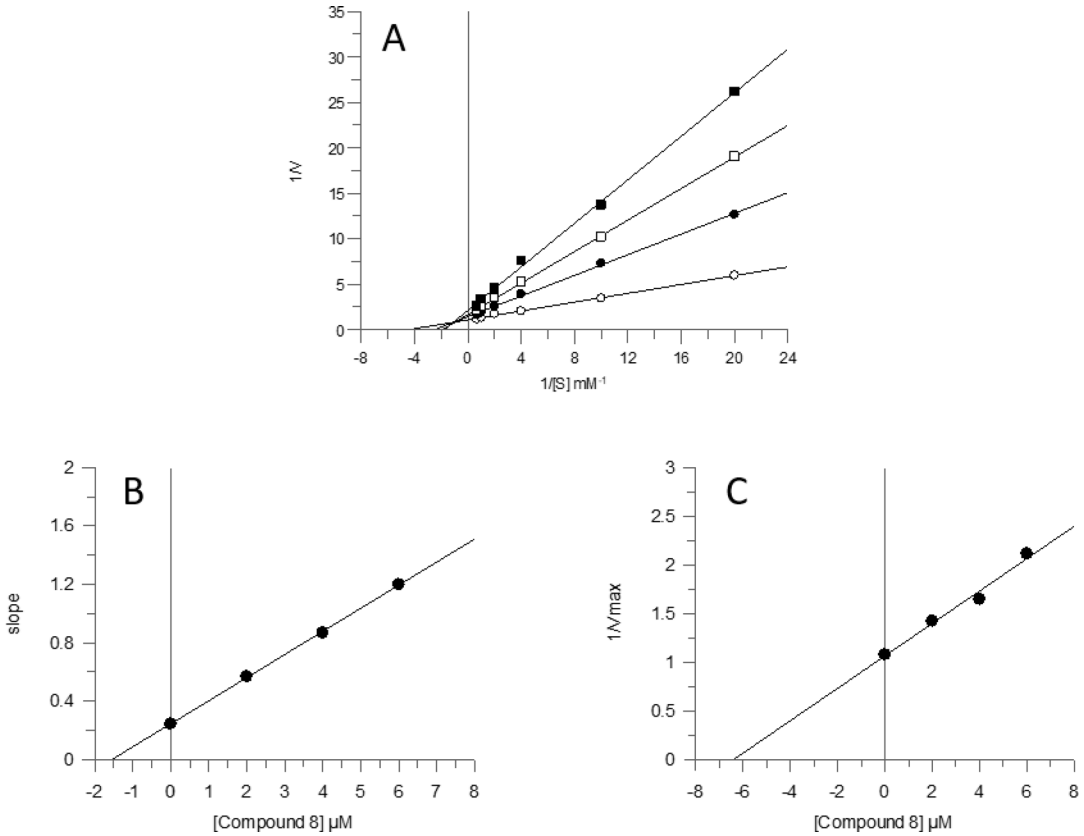


Fig. 1 Inhibition of BChE by compound **8**. (**A**) Lineweaver–Burk analysis; concentrations of compound were 0 (open circle), 2 (black filled circle), 4 (open square) and 6 (black filled square) µM. (**B,C**) Secondary plots for the calculation of K_I (**B**) and K_{IS} (**C**).

Cell viability in SH-SY5Y and cellular antioxidant activity

Compounds **8** and **12**, identified as the most potent BChE inhibitors and promising molecules, were further evaluated for their cytotoxicity in SH-SY5Y cells. As shown in Fig. 3, compound **8** had no significant effect on cell viability over the concentration range tested, maintaining viability above 80% even at the highest concentration (50 µM). In contrast, compound **12** showed a slight concentration-dependent decrease in cell viability, which remained around 80% at 25 µM, while 50 µM reduced viability to approximately 60%. Therefore, subsequent cell-based experiments were performed using concentrations up to 50 µM for compound **8** and up to 25 µM for compound **12**.

Given the key role of redox imbalance in the development and progression of AD, the antioxidant potential of compounds **8** and **12** was subsequently investigated by evaluating their ability to reduce ROS generation induced by H_2O_2 in SH-SY5Y cells. Cells exposed to H_2O_2 alone showed a marked increase in intracellular ROS levels (Fig. 4). Treatment with both compounds resulted in a significant dose-dependent reduction in H_2O_2-induced ROS production, confirming the validity of the oxidative stress model. Compound **8** had no significant effect at 1–10 µM, while a concentration-dependent reduction in ROS levels was determined at 25 and 50 µM. Compound **12** showed a slightly different profile, as a clear dose-dependent reduction in ROS production was observed at 5 µM, with a further decrease up to 25 µM, corresponding to its maximum non-cytotoxic concentration.

Overall, these results indicate that compounds **8** and **12** reduce intracellular ROS production, although with slightly different potency. Compound **12** appears to exert a higher antioxidant effect at lower concentrations than compound **8**, suggesting a higher cellular potency in this assay. Taken together, these findings corroborate

https://doi.org/10.1038/s41598-026-79845-9

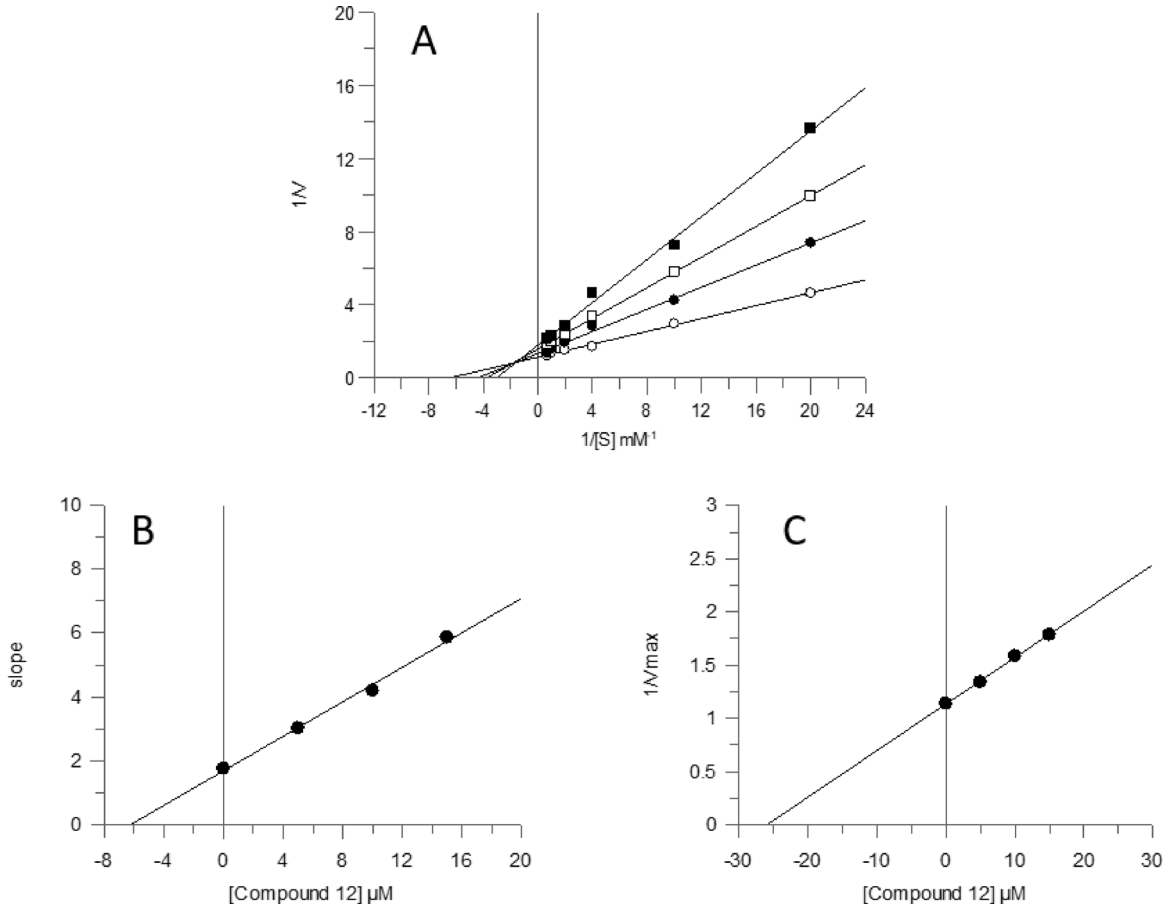


Fig. 2 Inhibition of BChE by compound **12**. (**A**) Lineweaver–Burk analysis; compound concentrations were 0 (open circle), 5 (black filled circle), 10 (open square) and 15 (black filled square) µM. (**B,C**) Secondary plots for the calculation of K_I (**B**) and K_{IS} (**C**).

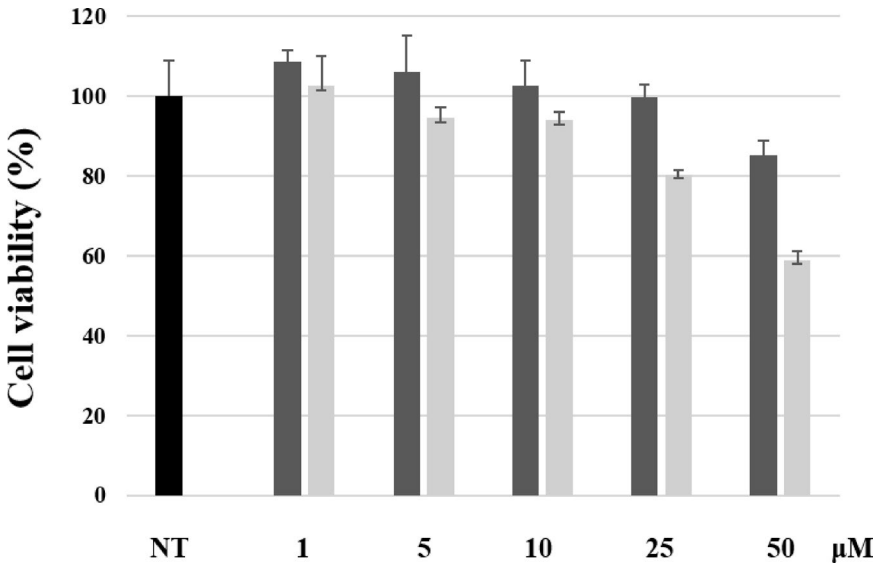


Fig. 3 Effect of the most active compounds **8** (dark gray filled square) and **12** (light gray filled square) on SH-SY5Y cells. Cell viability was presented as a percentage of the untreated control (NT). Data represented the mean ± standard deviation of six independent experiments.

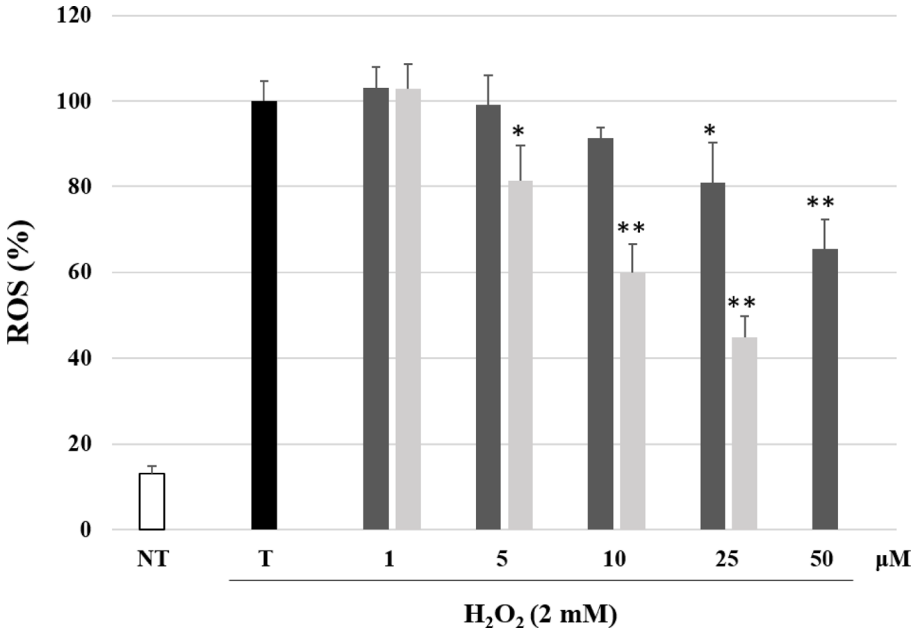


Fig. 4 Effect of compounds **8** (dark gray filled square) and **12** (light gray filled square) on H2O2-induced ROS generation in SH-SY5Y cells. NT, non-treated cells (white column) and T, cells treated with H2O2 only (black). Results are expressed as mean ± standard deviation from six independent experiments. Group comparisons were carried out using one-way ANOVA, with Tukey's applied for post hoc multiple comparisons. Significant differences from NT are marked with asterisks. Compound 8 is statistically different from T at 25 µM ($p = 0.0052$) and 50 µM ($p < 0.0001$), while compound 12 shows a significant difference compared to T at 5 µM ($p = 0.0065$), 10 µM and 25 µM ($p < 0.0001$).

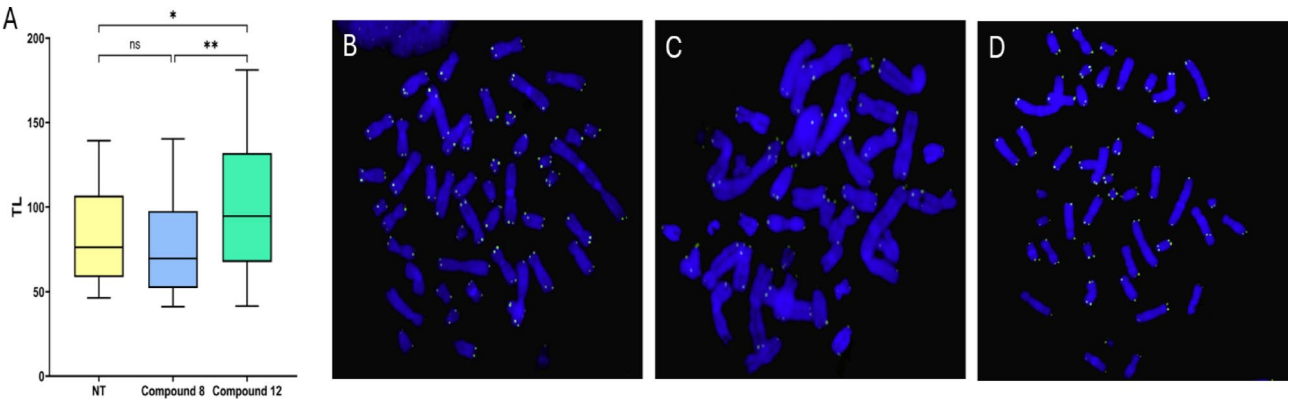


Fig. 5 Differences in telomere length and metaphase fluorescence intensity of telomeres under different conditions. The histogram illustrates the variation in telomere length (TL) among not treated (NT), treated with compound **8**, and treated with compound **12** cells (**A**). Bars indicate the mean and standard error of the mean. *$p < 0.05$; **$p < 0.005$. Fluorescence intensity of telomeres in NT (**B**), in cells treated with compound **8** (**C**), and in cells treated with compound **12** (**D**). Telomere probe (green); metaphases stained with DAPI (blue).

previously obtained results, confirming the biological activity of both molecules and providing further support to the observations regarding their inhibitory capacity towards BChE.

Telomere length in SH-SY5Y

Comparison of the experimental conditions revealed significant differences in telomere fluorescence intensity (Fig. 5). Specifically, cells treated with compound **12** exhibited significantly higher telomere fluorescence intensity (101.5 ± 37 AU) than both compound **8**-treated cells (77.1 ± 27.2 AU; $p = 0.0016$) and untreated cells (NT: 83.6 ± 27.4 AU; $p = 0.03$). Conversely, cells exposed to compound **8** exhibited no significant differences relative to NT ($p = 0.63$). Compound **12** was the only derivative that significantly increased telomere fluorescence intensity compared that to in both untreated cells and compound **8**-treated cells. Although 24-h treatment is unlikely to induce true telomere elongation, increased telomere fluorescence intensity is indicative of better preservation

of telomeric integrity. This finding is consistent with the superior antioxidant properties of compound **12**, which exhibited the lowest EC_{50} value in the ABTS assay and a more pronounced reduction in intracellular ROS compared to compound **8**. Since oxidative stress easily targets telomeric DNA, improved telomeric fluorescence may reflect reduced oxidative injury rather than changes in telomere length, in line with previous evidence linking antioxidant protection to telomere preservation [21].

Inhibition of the formation of Aβ42 aggregates

To detect and measure Aβ-42 amyloid fibrils, compounds **8** and **12** were tested using the ThT assay (Fig. 6). Compound **8** showed a dose-dependent inhibitory profile for fibril formation. In fact, while the Aβ-42 to compound ratios of 1:0.01 and 1:0.1 only slightly delayed the onset of aggregation, the 1:1 ratio prolonged the lag phase

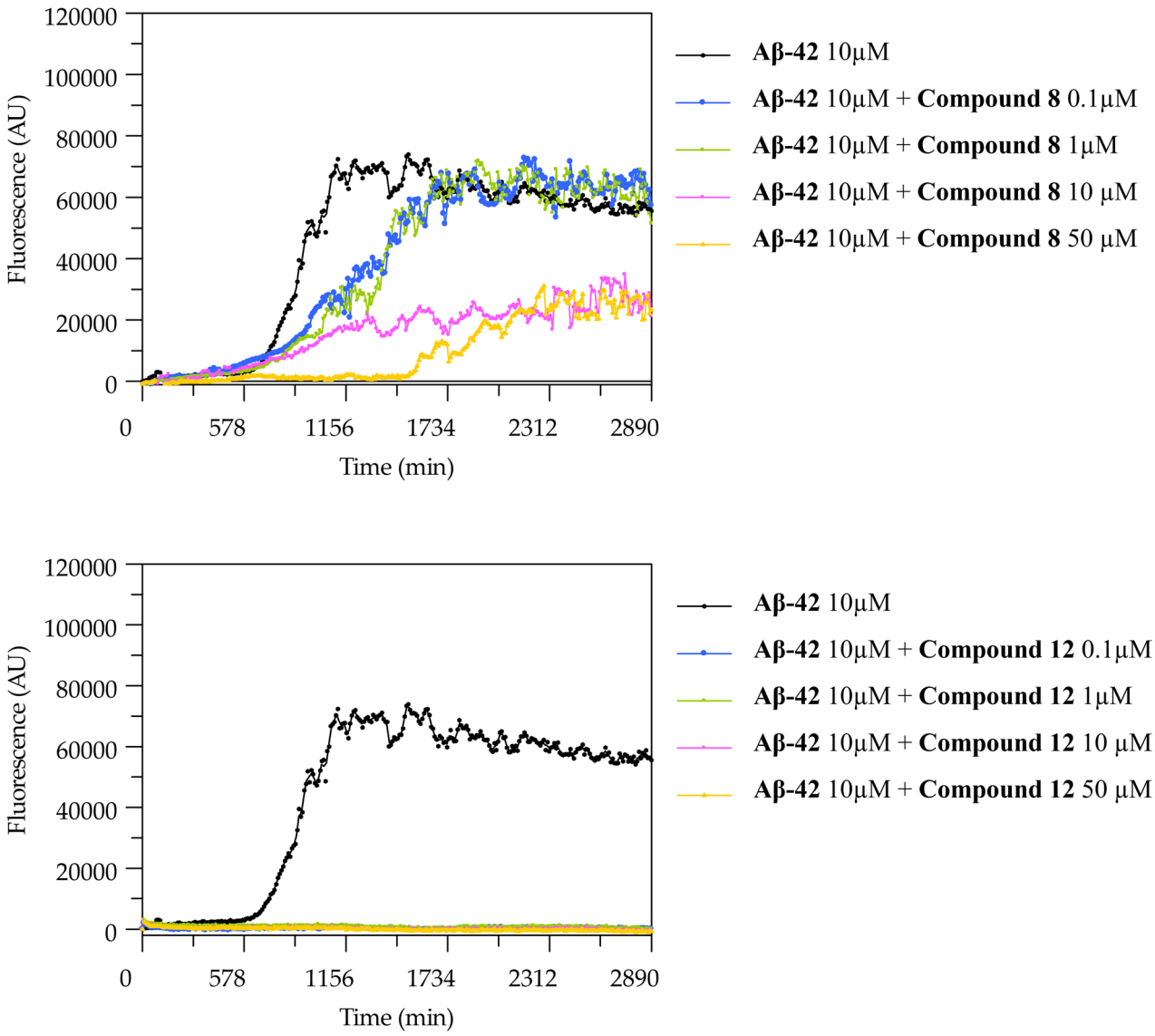


Fig. 6 ThT fluorescence curves (AU) plotted over time (min) showing the dose-dependent effect of compound **8** (upper panel) and compound **12** (lower panel) on Aβ42 aggregation. In both graphs, the black curve represents the Aβ42 alone control, while the remaining curves illustrate the co-incubation of Aβ42 with the respective compound at the following molar ratios (Aβ42: compound): 1:0.01 (blue), 1:0.1 (green), 1:1 (magenta), and 1:5 (yellow).

and partially reduced the plateau intensity. A more pronounced effect was observed at the higher 1:5 ratio, which markedly suppressed the final fluorescence plateau, highlighting that the inhibition is concentration-dependent. Conversely, compound **12** demonstrated strong potency against Aβ42 self-assembly: the corresponding curves appeared completely flat and superimposed near the baseline across all tested ratios down to the lowest concentration, indicating that there is a complete suppression of fibril formation and that the cross-β sheet architecture is fully abrogated.

Transmission Electron Microscopy (TEM) was used to complement the kinetic data and assess the morphology of the endpoint Aβ42 aggregates. TEM images of the control sample revealed a dense, interconnected meshwork of mature, elongated, and well-defined amyloid fibrils (Fig. 7A). In contrast, samples incubated with compound **8** exhibited a complete absence of ordered fibrillar networks and the predominance of large, bulky, and highly disordered amorphous aggregates, which confirms that the aggregation process is redirected toward an alternative, off-pathway precipitation mechanism rather than the fibrillation pathway (Fig. 7B). Conversely, samples treated with compound **12** displayed a complete suppression of mature polymeric fibril formation and the exclusive presence of small, highly monodisperse spherical assemblies, indicating that the compound stabilizes the peptide in early, non-fibrillar ThT-silent oligomeric states (Fig. 7C).

ADMET screening (absorption, distribution, metabolism, and excretion)

Compounds are generally considered drug-like and exhibit favourable pharmacokinetic properties when they satisfy the criteria outlined by Lipinski's Rule of Five. The potential AChE and BChE inhibitors (**8–12**) were evaluated using the SwissADME [18] and ADMETlab 3.0 programs [22]. Table 2 summarizes the physicochemical, lipophilic, and pharmacokinetic properties calculated after applying multiple filters [23–27].

The molecular weights of the compounds range from 224 to 305 g/mol, a range generally considered optimal for drug-likeness ($150 \leq MW \leq 500$ g/mol). Similarly, their Topological polar surface areas (TPSA) range from 33.37 to 53.60 $Å^2$, well within the generally approved range of 20–130 $Å^2$ for drug-like molecules.

The number of hydrogen bond acceptors (HBA) and donors (HBD) varies between 2 and 3 and 1–2, respectively, consistent with favourable values for drug candidates ($HBA \leq 10$; $HBD \leq 5$). In the benzofuran derivatives **8–12**, the fraction of sp^3-hybridized carbon atoms is below 0.25, reflecting a relatively rigid but well-defined molecular framework.

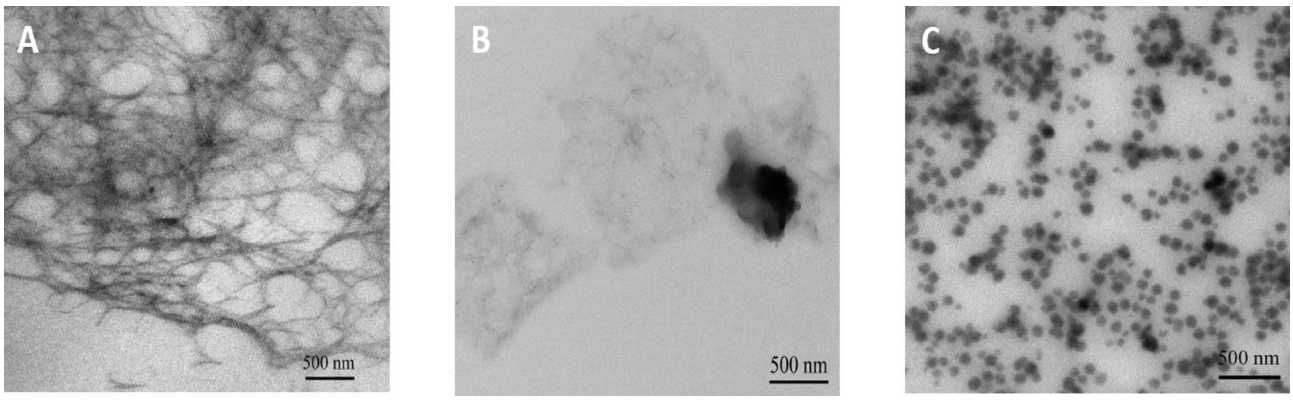


Fig. 7 Electron microscopy examination of the material obtained after ThT analysis: (**A**) Control sample showing a dense network of well-defined, mature Aβ42 fibrils; (**B**) Aβ42 in the presence of compound **8** at ratio 1:5, characterized by large, amorphous and disordered protein aggregates with no visible fibrillar structures; (**C**) Aβ42 in the presence of compound **12** at ratio 1:0.01, showing total inhibition of fibrillogenesis and the exclusive presence of spherical, oligomeric particles.

Table 2 Physicochemical and pharmacokinetic characteristics of compounds **8**–**12**.

		Compounds				
		8	**9**	**10**	**11**	**12**
Physicochemical properties	MW (g/mol)	224.25	224.25	240.25	260.67	305.12
	HBA	2	2	3	3	3
	HBD	1	1	2	2	2
	TPSA (Å^2)	33.37	33.37	53.60	53.60	53.60
Lipophilicity	iLog*P*	2.49	2.59	2.38	2.46	2.58
Water solubility	Log*S* (ESOL)	-4.34	-4.34	-4.17	-4.46	-4.78
	Solubility	MS	MS	MS	MS	MS
Pharmacokinetics	GI absorption	high	high	high	high	high
	BBB permeant	yes	yes	yes	yes	yes
	LogKp (cm/s)	-4.83	-4.83	-5.18	-5.12	-5.34
Druglikeness	Lipinski violations	0	0	0	0	0
	Ghose violations	0	0	0	0	0
	Veber violations	0	0	0	0	0
	Egan violations	0	0	0	0	0
	Muegge violations	0	0	0	0	0
	Bioavailability Score (F)	0.55	0.55	0.55	0.55	0.55

Molecular weight: MW, HBD: hydrogen bonds donor, HBA: hydrogen bond acceptor, TPSA: topological polar surface area, iLogP values: indicator of lipophilicity, ESOL: aqueous solubility parameter, MS: moderately soluble; Log Kp: skin permeation, F: bioavailability score.

Lipophilicity, expressed as iLog*P*, spans 2.38–2.59, suggesting moderate lipophilicity suitable for oral absorption. Water solubility, evaluated using the ESOL model [28], classifies all compounds as moderately soluble (LogS: -4.34 to -4.78).

Pharmacokinetic assessments suggest that all compounds exhibit high intestinal (GI) absorption and can permeate the blood–brain barrier (BBB).

All compounds comply with Lipinski, Ghose, Veber, Egan, and Muegge rules, exhibiting no violations and a consistent bioavailability score (F) of 0.55, indicating favorable oral bioavailability.

Overall, these properties demonstrate that compounds **8**–**12** possess a balanced profile of solubility, permeability, and drug-likeness, supporting their potential as orally active CNS-targeting agents.

The BOILED-Egg (Brain Or IntestinaL EstimateD) is a simple predictive approach based on log*P* and TPSA parameters that predicts human gastrointestinal absorption (HIA) and BBB permeability [29]. The yolk (yellow region) indicates a high probability of brain penetration, while the white region (intestinal tract) represents a high likelihood of passive gastrointestinal absorption. Plotting WLOGP and TPSA values on the BOILED-Egg diagram (Fig. 8) showed that all compounds fell within the yolk region, suggesting a physicochemical profile consistent with both high gastrointestinal absorption and predicted brain penetration. This distribution suggests a potential for BBB penetration and access to the central nervous system.

In silico toxicity evaluation, performed using ADMETlab 3.0 [22], suggests that compounds **8**–**12** are unlikely to act as human ether-a-go-go-related gene (hERG) blockers, indicating a low risk of cardiotoxicity. AMES mutagenicity tests and acute oral toxicity are predicted to be moderate across the series, while carcinogenicity remains generally low to moderate. Among the compounds, derivative **12** shows the most favorable overall toxicity profile, making it a particularly interesting candidate for further investigation. Overall, these results point to an acceptable safety profile, although experimental validation is still required (Table 3).

Molecular docking study

Based on their promising biological activity, compounds **8** and **12** were selected for molecular docking studies in AChE and BChE. The docking results provided valuable insights into the key interactions responsible for

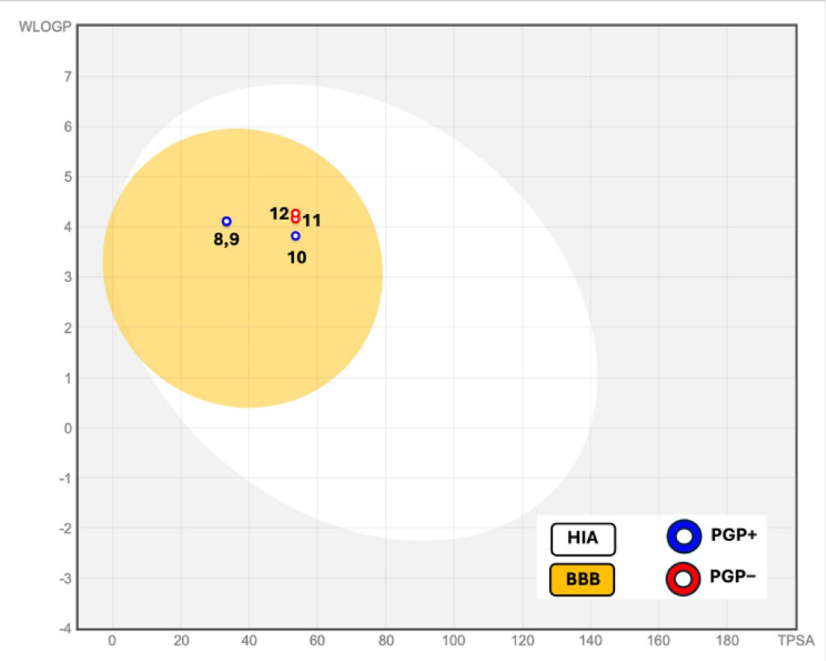


Fig. 8 BOILED-Egg diagram for the compounds evaluated in this study.

Table 3 Virtual toxicological properties of benzofurans **8**–**12**.

Compounds	8	9	10	11	12
hERG blockers	0.156	0.127	0.105	0.194	0.138
	--	--	--	--	--
AMES toxicity	0.519	0.575	0.584	0.412	0.356
	+	+	+	-	-
Rat oral acute toxicity	0.403	0.45	0.424	0.449	0.511
	-	-	-	-	+
Carcinogenicity	0.781	0.822	0.742	0.662	0.695
	++	++	++	+	+

hERG: human Ether-a-go-go-Related Gene; AMES: AMES test

--- (0-0.1); -- (0.1–0.3); - (0.3–0.5); + (0.5–0.7); ++ (0.7–0.9); +++ (0.9-1.0)

the enzyme binding. The presence of two hydroxyl groups in benzofuran **12** allows for the formation of three hydrogen bonds. The hydroxyl group at position 3' acts as a hydrogen bond donor with both Glu197 and Gly115. Furthermore, compound **12** interacts with Trp82, which is part of the anionic site of the enzyme, thanks to a hydrophobic interaction and π-stacking (Fig. 9).

In the benzofuran **8**, the hydroxyl group at position 3' is only able to interact with Gly78, acting as a hydrogen bond donor. Interactions with amino acids as part of the anionic site are also lost due to the different poses that the ligand adopts in the binding site. This may be due to the lipophilicity of the methyl group at position 5 of the scaffold, which forces compound **8** to take a conformation that allows for the protrusion of this substituent out of the active catalytic site (Fig. 10), interacting with Pro285. This moves the molecule to the peripheral anionic site (PAS) and allows for interactions with amino acids such as Tyr332. PAS structure differences between AChE and BuChE [30] may explain the difference in activities observed for benzofuran **8** among both enzymes. Finally, compound **8** is predicted to establish a hydrophobic interaction with His438, part of the catalytic triad. These interactions might lead to lower IC_{50} values, as opposed to those of other compounds within the series.

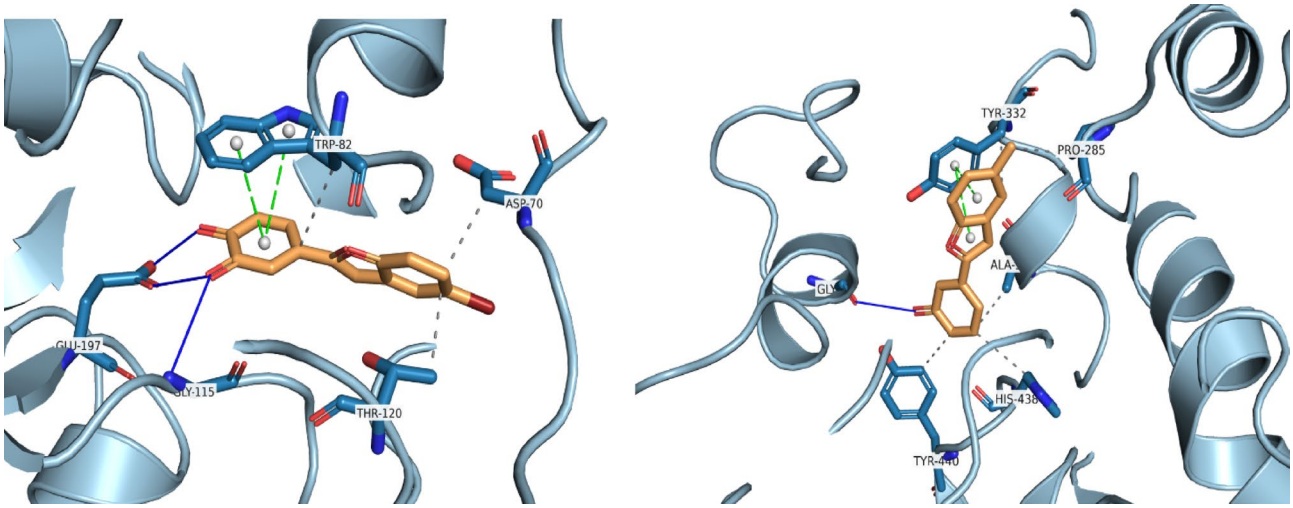


Fig. 9 PLIP-derived interaction maps for compounds **12** (left) and **8** (right) bound to BChE, rendered in PyMOL. The protein appears as a blue cartoon and the ligands as sticks with orange carbons and element-coloured heteroatoms; labels mark the contacting residues. Dashed green lines denote π-stacking, with the centroids of the stacked rings indicated by white spheres; dashed grey lines denote hydrophobic contacts and solid blue lines hydrogen bonds.

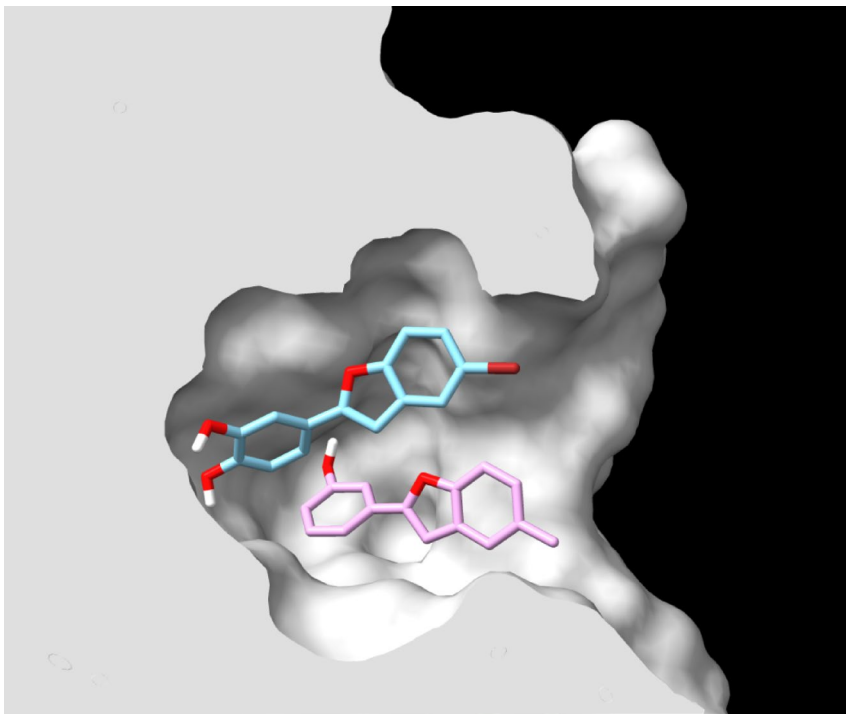


Fig. 10 Predicted best pose in BChE pocket for both ligands (benzofuran **12** in blue and benzofuran **8** in pink; hydrophobic surface of BChE represented in white).

Conclusions

This study demonstrated that hydroxylated 2-phenylbenzofurans hold potential as a scaffold for developing molecules that can target multiple aspects of AD. Rather than acting on a single pathological pathway, these novel derivatives successfully link three key hallmarks of AD pathogenesis: cholinergic dysfunction, amyloid-beta aggregation, and oxidative stress-induced neurodegeneration. Among the series, compounds **8** and **12** emerged as potent, mixed-type BChE inhibitors. The molecular docking analysis clarified this behaviour, suggesting their

potential to concurrently interact with both CAS and PAS. Notably, this research highlights the multi-target profile of compound **12**. At cellular level, it exerted a neuroprotective effect in SH-SY5Y cells by significantly suppressing hydrogen peroxide-induced ROS accumulation at non-cytotoxic doses. This potent antioxidant capacity was further reflected in its ability to protect telomeric integrity against oxidative damage. Crucially, kinetic and morphological evaluations via ThT assay and TEM revealed that compound **12** completely prevented Aβ42 fibril formation even at the lowest tested concentration. Taken together with its favourable predicted pharmacokinetic, drug-likeness and blood-brain barrier permeability profiles, these findings identified compound **12** as a promising candidate for further investigation and optimization.

Despite these encouraging findings, further studies are needed to validate the in vivo efficacy and safety of compound **12** and to better characterize its pharmacokinetic properties. In particular, the molecular mechanisms underlying its neuroprotective, antioxidant, and anti-amyloidogenic effects remain to be elucidated. Future studies will also focus on optimizing the 2-phenylbenzofuran scaffold to support its potential as a multi-target-directed ligand for Alzheimer's disease therapy.

Supplementary Information The online version contains supplementary material available at https://doi.org/10.1038/s41598-026-79845-9.

Acknowledgements We acknowledge the CeSAR (Centro Servizi Ricerca d'Ateneo) core facility of the University of Cagliari, Italy, G. Ferino and S. Lampis for assistance with the generation of HRMS mass and NMR spectra and Dr. Andrea Ardu for assistance with the generation of transmission electron microscopy images. Manuel Novás acknowledges financial support from a PhD fellowship awarded by Fundación Ramón Areces.

Author contributions G. L. D.: Conceptualization, Formal analysis, Investigation, Methodology, Writing – original draft, Writing – review and editing; M.B.: Investigation, Methodology; M.N.: Investigation, Software; M. J. M.: Funding acquisition, Investigation, Methodology, Writing – review and editing; P. C.: Investigation, Writing – review and editing; D. V. F.: Investigation, Visualization; V. S.: Investigation, Writing – review and editing; M. I.: Investigation, Visualization; C.S.: Visualization, Writing – review and editing; C. G. I. T.: Methodology, Writing – review and editing; (A) F.: Formal analysis, Writing – review and editing; (B) E.: Investigation, Writing – review and editing; S.F.: Conceptualization, Formal analysis, Investigation, Methodology, Writing – original draft, Writing – review and editing; F. P.: Conceptualization, Formal analysis, Funding acquisition, Investigation, Writing – original draft, Writing – review and editing.

Funding This research was funded by Fondazione di Sardegna (2022), Project ID: F73C23001850007. This project was also supported by Xunta da Galicia Grant (ED431B 2025/15).

Data availability All data supporting the findings of this study are available within the paper and its Supplementary Information.

Declarations

Competing interests The authors declare no competing interests.

Open Access This article is licensed under a Creative Commons Attribution 4.0 International License, which permits use, sharing, adaptation, distribution and reproduction in any medium or format, as long as you give appropriate credit to the original author(s) and the source, provide a link to the Creative Commons licence, and indicate if changes were made. The images or other third party material in this article are included in the article's Creative Commons licence, unless indicated otherwise in a credit line to the material. If material is not included in the article's Creative Commons licence and your intended use is not permitted by statutory regulation or exceeds the permitted use, you will need to obtain permission directly from the copyright holder. To view a copy of this licence, visit http://creativecommons.org/licenses/by/4.0/.

References

1. Safiri, S. et al. Alzheimer's disease: a comprehensive review of epidemiology, risk factors, symptoms diagnosis, management, caregiving, advanced treatments and associated challenges. *Front. Med.* **11**. https://doi.org/10.3389/fmed.2024.1474043 (2024).
2. Andrews, J. S. et al. Disease severity and minimal clinically important differences in clinical outcome assessments for Alzheimer's disease clinical trials. *Alzheimers Dement.* **5**, 354–363. https://doi.org/10.1016/j.trci.2019.06.005 (2019).
3. Greig, N. H., Lahiri, D. K. & Sambamurti, K. Butyrylcholinesterase: an important new target in Alzheimer's disease therapy. *Int. Psychogeriatr.* **14**, 77–91. https://doi.org/10.1017/s1041610203008676 (2002).
4. Nordberg, A., Ballard, C., Bullock, R., Darreh-Shori, T. & Somogyi, M. A review of butyrylcholinesterase as a therapeutic target in the treatment of Alzheimer's disease. *Prim. Care Companion CNS Disord*. **15**. https://doi.org/10.4088/pcc.12r01412 (2013).
5. Iliyasu, M. O., Musa, S. A., Oladele, S. B. & Iliya, A. I. Amyloid-beta aggregation implicates multiple pathways in Alzheimer's disease: Understanding the mechanisms. *Front. Neurosci.* **17**. https://doi.org/10.3389/fnins.2023.1081938 (2023).
6. Tönnies, E. & Trushina, E. O. Stress synaptic dysfunction, and Alzheimer's disease. *J. Alzheimers Dis.* **57**, 1105–1121. https://doi.org/10.3233/jad-161088 (2017).
7. Mesiti, F., Chavarria, D., Gaspar, A., Alcaro, S. & Borges, F. The chemistry toolbox of multitarget-directed ligands for Alzheimer's disease. *Eur. J. Med. Chem.* **181**, 111572. https://doi.org/10.1016/j.ejmech.2019.111572 (2019).
8. Von Zglinicki, T. Oxidative stress shortens telomeres. *Trends Biochem. Sci.* **27**, 339–344. https://doi.org/10.1016/s0968-0004(02)02110-2 (2002).
9. Delogu, G. L. et al. Structural insight of new butyrylcholinesterase inhibitors based on benzylbenzofuran scaffold. *Pharmaceuticals (Basel)* **15**, 304. https://doi.org/10.3390/ph15030304 (2022).
10. Fais, A. et al. Synthesis, molecular docking and cholinesterase inhibitory activity of hydroxylated 2-phenylbenzofuran derivatives. *Bioorg. Chem.* **84**, 302–308. https://doi.org/10.1016/j.bioorg.2018.11.043 (2019).
11. Kumar, A. et al. Novel 2-pheynlbenzofuran derivatives as selective butyrylcholinesterase inhibitors for Alzheimer's disease. *Sci. Rep.* **8**, 4424. https://doi.org/10.1038/s41598-018-22747-2 (2018).
12. Delogu, G. L. et al. 2-Phenylbenzofuran derivatives as butyrylcholinesterase inhibitors: Synthesis, biological activity and molecular modeling. *Bioorg. Med. Chem. Lett.* **26**, 2308–2313. https://doi.org/10.1016/j.bmcl.2016.03.039 (2016).
13. Delogu, G. L. et al. A new biological prospective for the 2-phenylbenzofurans as inhibitors of α-glucosidase and of the islet amyloid polypeptide formation. *Int. J. Biol. Macromol.* **169**, 428–435. https://doi.org/10.1016/j.ijbiomac.2020.12.117 (2021).
14. Delogu, G. L. et al. 2-Arylbenzofurans as selective cholinesterase inhibitors: design, synthesis, and evaluation as Alzheimer's disease agents. *Biomolecules* **16**, 178. https://doi.org/10.3390/biom16010178 (2026).
15. Era, B. et al. Anti-aging potential of extracts from Washingtonia filifera seeds. *Plants (Basel)* **10**, 151. https://doi.org/10.3390/plants10010151 (2021).
16. Squassina, A. et al. Telomere attrition and inflammatory load in severe psychiatric disorders and in response to psychotropic medications. *Neuropsychopharmacology* **45**, 2229. https://doi.org/10.1038/s41386-020-00844-z (2020).
17. Levine, H. Thioflavine T interaction with synthetic Alzheimer's disease beta-amyloid peptides: detection of amyloid aggregation in solution. *Protein Sci.* **2**, 404. https://doi.org/10.1002/pro.5560020312 (1993).
18. Daina, A., Michielin, O. & Zoete, V. SwissADME: a free web tool to evaluate pharmacokinetics, drug-likeness and medicinal chemistry friendliness of small molecules. *Sci. Rep.* **7**, 42717. https://doi.org/10.1038/srep42717 (2017).
19. Xiong, G. et al. ADMETlab 2.0: an integrated online platform for accurate and comprehensive predictions of ADMET properties. *Nucleic Acids Res.* **49**, W5–W14. https://doi.org/10.1093/nar/gkab255 (2021).
20. Eberhardt, J., Santos-Martins, D., Tillack, A. F. & Forli, S. AutoDock Vina 1.2.0: new docking methods, expanded force field, and python bindings. *J. Chem. Inf. Model.* **61**, 3891–3898. https://doi.org/10.1016/j.mad.2018.03.013 (2021).
21. Barnes, R. P., Fouquerel, E. & Opresko, P. L. The impact of oxidative DNA damage and stress on telomere homeostasis. *Mech. Ageing Dev.* **177**, 37–45. https://doi.org/10.1016/j.mad.2018.03.013 (2019).
22. Fu, L. et al. ADMETlab 3.0: an updated comprehensive online ADMET prediction platform enhanced with broader coverage, improved performance, API functionality and decision support. *Nucleic Acids Res.* **52**, W422–W431. https://doi.org/10.1093/nar/gkae236 (2024).
23. Lipinski, C. A., Lombardo, F., Dominy, B. W. & Feeney, P. J. Experimental and computational approaches to estimate solubility and permeability in drug discovery and development settings. *Adv. Drug Deliv. Rev.* **46**, 3–26. https://doi.org/10.1016/s0169-409x(00)00129-0 (2001).
24. Ghose, A. K., Viswanadhan, V. N. & Wendoloski, J. J. A knowledge-based approach in designing combinatorial or medicinal chemistry libraries for drug discovery. 1. A qualitative and quantitative characterization of known drug databases. *J. Comb. Chem.* **1**, 55–68. https://doi.org/10.1021/cc9800071 (1999).
25. Veber, D. F. et al. Molecular properties that influence the oral bioavailability of drug candidates. *J. Med. Chem.* **45**, 2615–2623. https://doi.org/10.1021/jm020017n (2002).

26. Egan, W. J., Merz, K. M. & Baldwin, J. J. Prediction of drug absorption using multivariate statistics. *J. Med. Chem.* **43**, 3867–3877. https://doi.org/10.1021/jm000292e (2000).
27. Muegge, I., Heald, S. L. & Brittelli, D. Simple selection criteria for drug-like chemical matter. *J. Med. Chem.* **44**, 1841–1846. https://doi.org/10.1021/jm015507e (2001).
28. Delaney, J. S. ESOL: estimating aqueous solubility directly from molecular structure. *J. Chem. Inf. Comput. Sci.* **44**, 1000–1005. https://doi.org/10.1021/ci034243x (2004).
29. Daina, A. & Zoete, V. A BOILED-Egg to predict gastrointestinal absorption and brain penetration of small molecules. *ChemMedChem* **11**, 1117–1121. https://doi.org/10.1002/cmdc.201600182 (2016).
30. MacDonald, I. R., Martin, E., Rosenberry, T. L. & Darvesh, S. Probing the peripheral site of human butyrylcholinesterase. *Biochemistry* **51**, 7046–7053. https://doi.org/10.1021/bi300955k (2012).

Publisher's note Springer Nature remains neutral with regard to jurisdictional claims in published maps and institutional affiliations.

Authors and Affiliations

Giovanna Lucia Delogu[1] · Michela Begala[1] · Manuel Novás[2,3] · Maria João Matos[2] · Paola Caria[4] · Daniela Virginia Frau[4] · Valeria Sogos[4] · Michela Isola[4] · Cinzia Sanna[5] · Carlo Giovanni Ignazio Tuberoso[1] · Antonella Fais[1] · Benedetta Era[1] · Sonia Floris[1] · Francesca Pintus[1]

✉ Sonia Floris
s.floris@unica.it

[1] Department of Live and Environmental Sciences, University of Cagliari, Cittadella Universitaria, SS 554, Km 4.5, 09042 Monserrato, Italy

[2] Departamento de Química Orgánica, Facultad de Farmacia, Universidade de Santiago de Compostela, Santiago de Compostela 15782, Spain

[3] BioFarma Research Group, Center for Research in Molecular Medicine and Chronic Diseases (CiMUS), University of Santiago de Compostela, Santiago de Compostela 15782, Spain

[4] Department of Biomedical Science, University of Cagliari, Cittadella Universitaria, SS 554, Km 4.5, Monserrato 09042, Italy

[5] Department of Live and Environmental Sciences, University of Cagliari, via sant 'Ignazio da Laconi 13, Cagliari 09123, Italy